ACS NANO

www.acsnano.org

ARTICLE

Atomic-Level Customization of Zinc Crystallization Kinetics at the Interface for High-Utilization Zn Anodes

Qin Liu, Xiong Liu, Yu Liu, Meng Huang, Weihao Wang, Yu Cheng, Hong Zhang, and Lin Xu*

Cite This: *ACS Nano* 2024, 18, 4932–4943

Read Online

ACCESS | Metrics & More | Article Recommendations | Supporting Information

ABSTRACT: **Understanding the crystallization occurring at the inner interfaces during electrochemical deposition is crucial for achieving a high reversibility in zinc anodes. However, design rules for crystallization kinetics still lack predictive power, particularly at the atomic scale, posing a significant challenge. Herein, we propose a crystal facet terminating agent, $LaCl_3$, which modulates the preferential crystallization orientation of Zn by regulating its growth kinetics through the synergistic adsorption of dual ions. Interface molecular dynamics (MD) simulations and crucial experimental parameters reveal that the strong (002) facet texture of Zn deposits primarily depends on the adsorption of strong inhibitors. Specifically, the high adsorption free energy of Cl^- on the Zn (002) facet and the concomitant aggregation of La^{3+} reduces the growth rate of the Zn (002) facet, thereby favoring its preservation as the final crystal facet. Consequently, this terminating agent enables the Zn anodes to deliver a high cumulative capacity of 12 Ah cm^{-2} at 40 mA cm^{-2}, 20 mAh cm^{-2}. The Zn||MnO_2 full cell, when coupled with a high-mass-loading cathode and limited Zn supply, can maintain a practical areal capacity of 3.39 mAh cm^{-2}. Furthermore, rigorous testing conditions and the successful scaling up to a 0.34 Ah pouch cell further confirm its promising prospects for practical applications.**

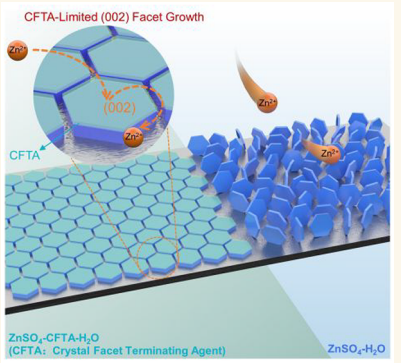

KEYWORDS: *CFTA, crystal growth kinetics, Zn texture, high-areal-capacity, Zinc-ion battery*

The rechargeable Zn-based aqueous battery (ZAB) is the most potential candidate for large-scale energy storage system, because of the advantages of Zn metal, including superior capacity (5854 Ah L^{-1}), low potential (−0.762 V vs the standard hydrogen electrode), and inherent safety.[1−3] Unfortunately, Zn anodes suffer from severe dendrites and irreversible byproducts, which lead to poor electrochemical reversibility, low Coulombic efficiency (CE), and limited battery lifespan.[4−7] Especially for practical applications, the long-term cycling stability of ZAB is more challenging under high depth of discharge (DOD) and high areal capacity.[8−10] Various strategies have been proposed to improve the reversibility of Zn anodes, including metal-host anode design (e.g., fluorinated alloy[11] or 3D porous frameworks[3,12]), epitaxial electrodeposition,[13] and (002)-surface-preferred Zn anodes.[14,15] However, these strategies rely on modification of Zn anodes, which limits them to subdued performance levels in practical application scenarios such as high areal capacity.[16] For instance, the design of 3D porous frameworks could help to inhibit dendrite growth by improving the uniformity of Zn flux, but the limited space of the 3D structure cannot achieve uniform deposition under the high-areal-capacity conditions.[3] Epitaxial deposition is effective for promoting preferential orientation growth, while the epitaxial effect will gradually weaken or even disappear under high areal capacity.[13] Therefore, it is highly desired to develop solutions to enable high reversibility and high DOD Zn anodes without relying on the current collector substrate and fundamentally solve the issues of uncontrollable Zn growth.

In the traditional aqueous $ZnSO_4$ electrolyte, numerous discrete Zn protrusions are generated on the Zn anode due to the uncontrollable growth rate and orientation of the crystal facet. The electric field tends to accumulate at the top of these Zn protrusions, which is attributed to the tip effect of the electric field, and this intense charge density distribution easily induces dendrite growth.[17] To realize homogeneous and smooth Zn plating, it is necessary to regulate the growth rate and behavior of specific crystal facets to avoid tip growth.

Received: October 23, 2023
Revised: January 18, 2024
Accepted: January 19, 2024
Published: January 29, 2024

https://doi.org/10.1021/acsnano.3c10394
ACS Nano 2024, 18, 4932–4943

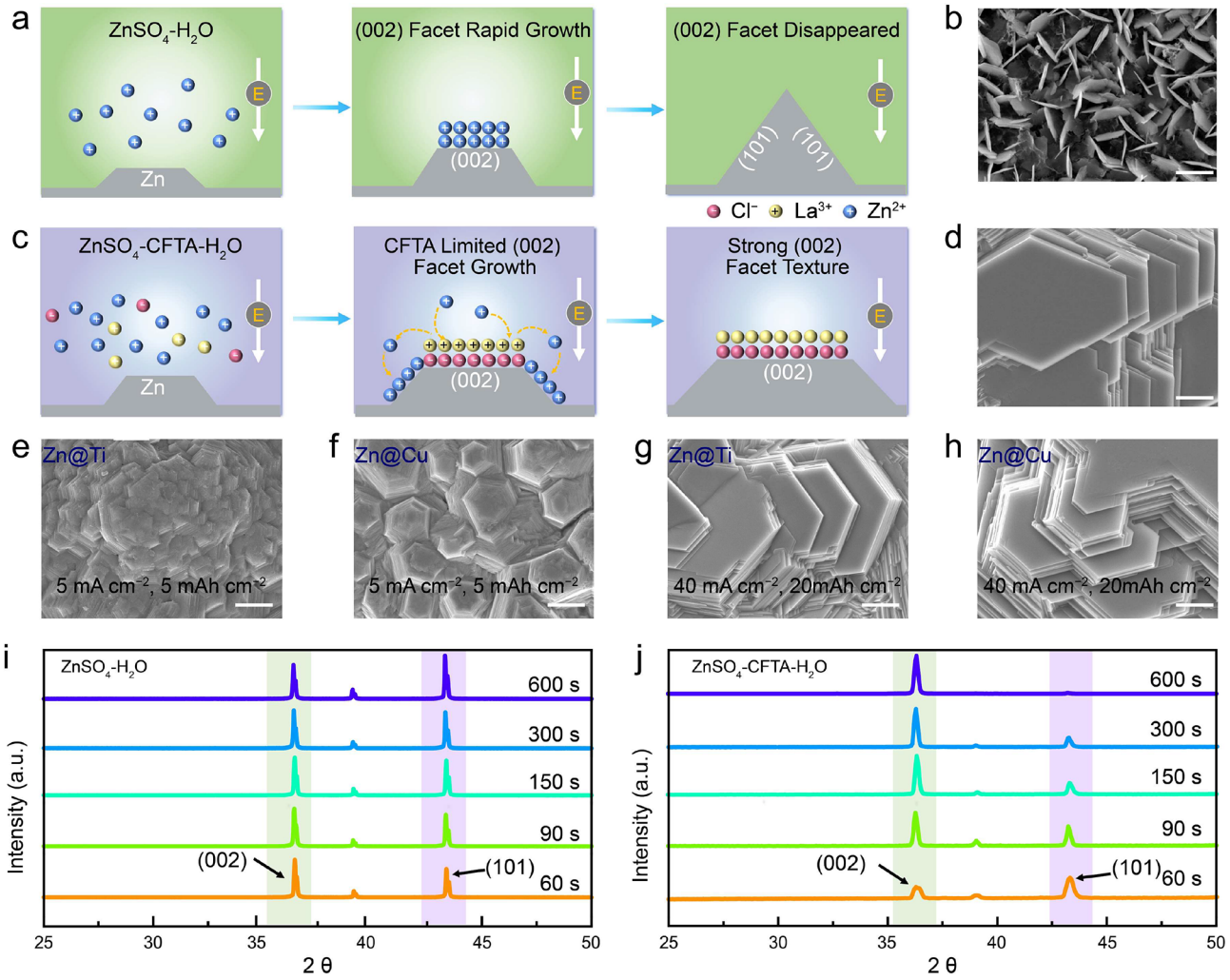

Figure 1. (a) Zn crystal growth process in $ZnSO_4$−H_2O system. (b) SEM image of Zn anode after cycled at 10 mA cm^{-2} in $ZnSO_4$−H_2O electrolyte. Scale bar = 10 μm. (c) Zn crystal growth process in $ZnSO_4$−CFTA−H_2O system. (d) SEM image of Zn anode after being cycled at 10 mA cm^{-2} in $ZnSO_4$−CFTA−H_2O electrolyte. Scale bar = 5 μm. (e, f) SEM images of the Zn electrodeposits at 5 mA cm^{-2}, 5 mAh cm^{-2} with Ti substrate (panel (e)) and Cu substrate (panel (f)). Scale bar = 10 μm. (g, h) SEM images of the Zn electrodeposits at 40 mA cm^{-2}, 20 mAh cm^{-2} with Ti substrate (panel (g)) and Cu substrate (panel (h)). Scale bar = 5 μm. (i, j) Ex situ SEM of Zn crystal growth behavior at 5 mA cm^{-2} in the $ZnSO_4$−H_2O electrolyte (panel (i)) and $ZnSO_4$−CFTA−H_2O (panel (j)).

Electrolyte modification strategy has been reported to be able to effectively change Zn deposition behavior and achieve uniform Zn deposition.[18−22] Note that electrolyte optimization is not limited to the deposition substrate and is the most promising approach to achieve a high DOD_{Zn} and highly chemically reversible Zn anodes simultaneously. Nevertheless, the above strategy faces some practical limitations, which make it unable to adapt to large-scale industrialization processes. Specifically, heavy-metal ions (Pb^{2+}, Bi^{3+}) and organic additives have severe environmental pollution and possible health hazards, which greatly restricts their application scenarios.[23,24] High concentration electrolytes sacrifice the ionic conductivity and rate performance due to high viscosity and lead to an increase in overall costs.[20,25−27] In addition, to the best of our knowledge, the above electrolyte modification is difficult to accurately regulate the crystal orientation of Zn deposition, which is crucial to further improving the stability of Zn anodes. Therefore, achieving customized crystallization kinetics for highly oriented growth of zinc crystals and fabricating high DOD_{Zn} anodes that can be used in practical applications remain a formidable task.

In this work, a crystal facet terminating strategy has been proposed assisted by dual ions to tailor electrolyte solvation structure and precisely control Zn deposition behavior under high Zn utilization rate. Lanthanum chloride ($LaCl_3$), a rare-earth-metal salt, has been demonstrated to be a crystal facet terminating agent (CFTA) for Zn crystals. In detail, the anionic group Cl^- can be specifically adsorbed on the (002) facet, while La^{3+} ions with lower reduction potentials tend to preferentially accumulate in the vicinity of Cl^- adsorption sites, reducing the growth kinetics of the (002) plane through electrostatic repulsion. Furthermore, the adsorption layer formed by the dual ions is not consumed during repeated Zn plating/stripping cycles, allowing for highly preferred (002) orientation growth even at high areal capacities. As a result, the cycling lifespan of ZABs has been significantly increased several times under practical conditions with high-loading cathodes and limited Zn anodes.

https://doi.org/10.1021/acsnano.3c10394
ACS Nano 2024, 18, 4932−4943

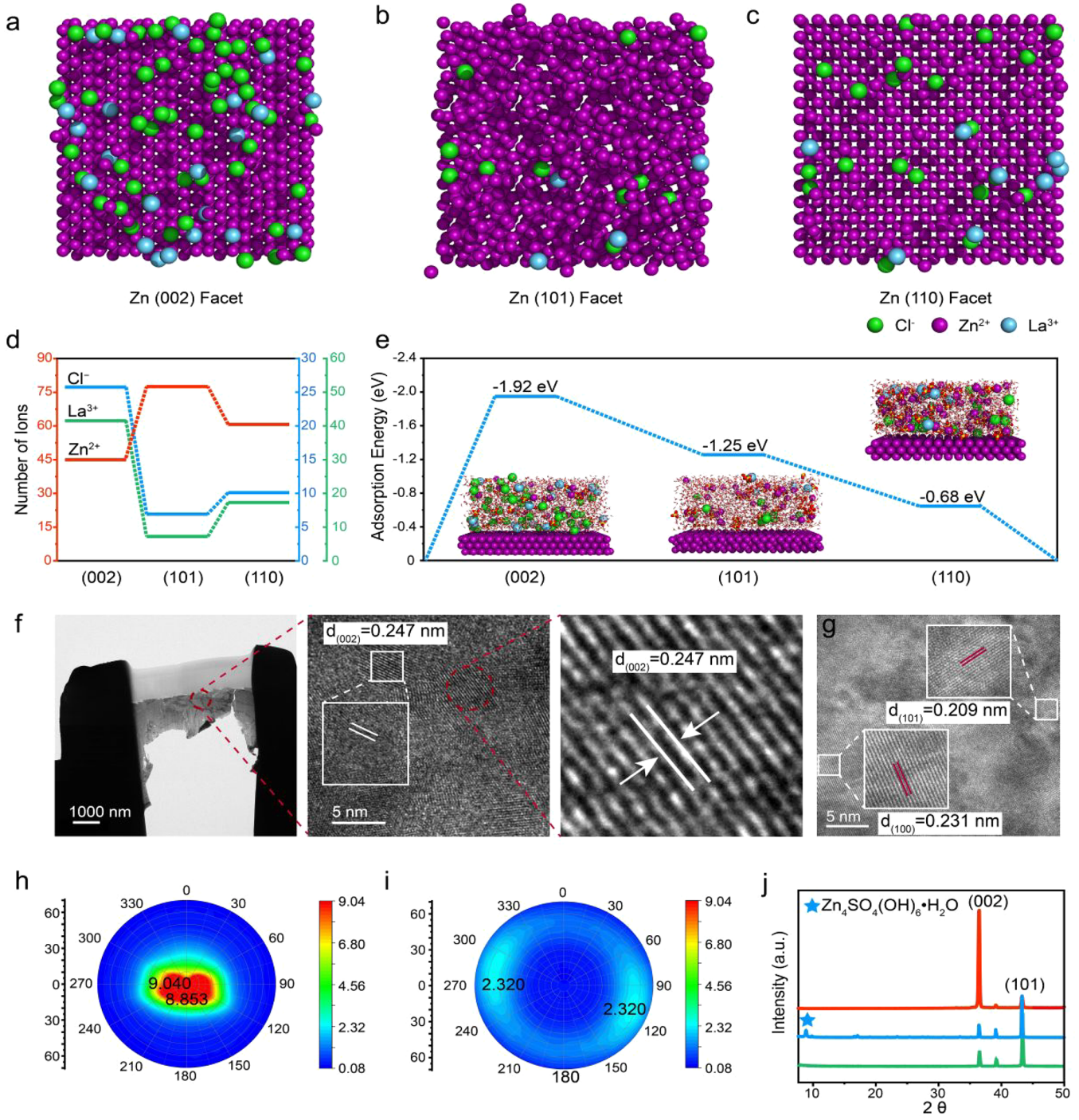

Figure 2. (a–c) Interfacial layering structure of different Zn facets obtained from MD simulations. (d) Analysis of the numbers of different ions in the innermost interfacial layer. (e) Adsorption free energy of Cl^- on different Zn facets. (f) TEM and HRTEM images of the hexagonal zinc deposits with $ZnSO_4$–CFTA–H_2O electrolyte. (g) HRTEM images of the hexagonal zinc deposits with $ZnSO_4$–H_2O electrolyte. (h, i) (002) facet pole figures of the Zn deposits in $ZnSO_4$–CFTA–H_2O electrolyte (panel (h)) and $ZnSO_4$–H_2O electrolyte (panel (i)). (j) XRD results of Zn deposits. [Legend: green spectrum, bare Zn; blue spectrum, Zn deposits in the $ZnSO_4$–H_2O electrolyte; and red spectrum, Zn deposits in $ZnSO_4$–CFTA–H_2O electrolyte.

RESULTS AND DISCUSSION

In the traditional pure $ZnSO_4$ electrolyte, the growth process of Zn crystals is shown in Figure 1a. Within the current density range of 1 to 100 mA cm^{-2}, the crystal growth behavior is mainly controlled by kinetics.[12] The (002) crystal facet exhibits a large exposure at the initial stage due to its low exponential and fast growth rate. However, according to the Bravais principle, with the progressive growth of the Zn crystal, the intensity of the rapidly growing (002) facet tends to gradually decrease, while the strength of the slowly growing (101) facet is expected to increase steadily over time. The crystal eventually exhibits anisotropy mainly dominated by the (101) and (002) planes with no obvious preferred orientation. As shown in Figure 1b, in pure $ZnSO_4$ electrolyte, the Zn deposits exhibit a disorderly dendritic morphology, which is

https://doi.org/10.1021/acsnano.3c10394
ACS Nano 2024, 18, 4932–4943

extremely harmful to the cycling stability of the ZABs. Herein, the incorporation of dual-ion CFTA, specifically $LaCl_3$, can modify the preferred orientation of Zn crystals by manipulating the crystal growth kinetics, as schematically illustrated in Figure 1c. In detail, Cl^- ions are preferentially adsorbed onto the (002) crystal facet of the Zn anode with a high coverage. The Cl^- adsorption sites on the (002) crystal facet, through electrostatic attraction, result in the formation of a rare-earth-ion adsorption layer containing La^{3+} on their surfaces. This layer displays strong electrostatic repulsion, preventing the movement of Zn^{2+} toward the (002) facet, resulting in a slowdown of the growth rate of the (002) facet and thereby enhancing the intensity of the (002) crystal facet. Due to the sustained effect of the CFTA additive, the Zn deposits exhibit dominant (002) facet orientation. Furthermore, while the Zn deposits gradually thicken, the Cl^- and La^{3+} ions continue to migrate toward the surface without impeding the subsequent Zn deposition process. As illustrated in Figure 1d, the Zn deposits exhibit a compact hexagonal morphology parallel to the substrate in the electrolyte containing dual-ion CFTA, indicating that the synergistic effect of Cl^- and La^{3+} can effectively regulate the growth kinetics during Zn plating and generate highly oriented Zn deposits.

To directly visualize the effects of the CFTA on the microstructure of Zn deposits, the transparent Zn||Zn symmetric cells using different electrolytes were assembled, and the Zn deposition processes were monitored in situ, using a combined electrochemical−optical system. Zn deposition was conducted at a current density of 5 mA cm^{-2} for 30 min (Figure S1). It has been observed that, in pure $ZnSO_4$ electrolyte ($ZnSO_4$−H_2O), the Zn deposits initially exhibit discrete protrusions with faster growth rates at the tips, primarily due to the sharp edge effect of the electric field. As the plating progresses, the Zn deposits gradually take on a loose structure, which can further increase the electrolyte consumption and promote the continuous growth of Zn dendritic protrusions (Figure S1a). Inversely, Zn deposits in the electrolyte containing CFTA ($ZnSO_4$−CFTA−H_2O) is smooth and no obvious Zn dendrites are observed even after 30 min, as evidenced in Figure S1b. The direct support for substrate-independent is obtained from (scanning electron microscopy) SEM images of Zn deposition morphologies on Cu and Ti substrates (Figures 1e−h). The SEM images show that the surfaces of both Cu and Ti substrates exhibit a similar Zn deposition morphology. The horizontally arranged hexagonal crystal particles have microsteps, and many microsteps connect to form a large area of dense film under electroplating conditions of 5 mA cm^{-2} and 5 mAh cm^{-2}. Under the high current density of 40 mA cm^{-2} and the large areal capacity deposition condition of 20 mAh cm^{-2}, the two substrates mentioned above exhibit similar horizontally arranged morphologies with larger hexagonal crystal particles. This indicates that the CFTA strategy can achieve a dense (002) Zn texture under high areal capacity and substrate-independent conditions. To investigate the evolution of the crystal facet preferred orientation during Zn deposition, ex situ SEM and X-ray diffraction (XRD) were performed in $ZnSO_4$−CFTA−H_2O electrolyte and $ZnSO_4$−H_2O electrolyte at a current density of 5 mA cm^{-2} for 10 min, respectively. In the $ZnSO_4$−H_2O electrolyte, the (002) facet exhibits a higher diffraction peak intensity than the (101) facet at the initial stage (Figure 1i). As the crystal grows over time, the diffraction peak at (101) becomes more prominent, and the SEM image shows a loose and flaky morphology (Figure S2), which is consistent with our proposal in Figure 1a that the slow growing (101) plane gradually strengthens. In the $ZnSO_4$−CFTA−H_2O electrolyte, the (101) facet of the initial Zn deposit has a high diffraction intensity, but the deposition behavior and orientation of Zn change significantly during the subsequent deposition process (Figure 1j). The (002) facet gradually becomes more pronounced and exhibits high preferred orientation. The Zn deposits exhibit a hexagonal morphology, growing parallel to the substrate direction and uniformly covering the surface of the Zn foil. Eventually, a relatively smooth, dense, and dendrite-free deposition morphology is obtained (Figure S3). Therefore, the introduction of CFTA into the pure $ZnSO_4$−H_2O system can effectively modulate the crystal growth behavior with the inhibition of Zn dendrites.

To reveal the influence mechanism of CFTA on Zn deposition behavior, molecular dynamics (MD) simulations were conducted by using ideal interface models. In these models, $ZnSO_4$ electrolyte supplemented with $LaCl_3$ is confined between two planar single-crystal Zn electrodes (Figure S4). The (002), (101), and (110) crystal facets of Zn are selected as single crystal electrodes, as they are prone to be exposed during the growth of Zn crystals (Figure 2a−c).[28] Compared to those of the (101) and (110) facets, the Cl^- and La^{3+} tend to accumulate and preferentially adsorb in the vicinity of the Zn(002) facet. The chemical composition of the innermost interface layer is further analyzed, via dividing the simulation box into two regions, namely, the area adjacent to the electrode surface within 23.2 Å and the bulk phase. The number of metal cations and halogen ions in the internal interface layer under all simulated crystal facets is plotted in Figure 2d. The number of La^{3+}/Cl^- ions in the innermost interface layer of (002), (101), and (110) facets are 22/50, 4/11, and 8/20, respectively.

The inner interface of the (002) facet has the highest concentration of Cl^- and La^{3+}, mainly because the increased Cl^- negative charge on the (002) facet makes the innermost La^{3+} cation enriched. Inversely, the numbers of Zn^{2+} in the inner layers of (002), (101), and (110) facets are 45, 78, and 63, respectively. Additionally, we performed zeta potential examination of the Zn anodes and differential capacitance curve tests. During the zeta potential measurement process, $ZnSO_4$−H_2O and $ZnSO_4$−CFTA−H_2O were utilized as electrolytes. Because of the experimental necessity of dispersing Zn within the electrolyte, commercial Zn powder was employed as a substitute for Zn foil. As shown in Figure S5, the zeta potential in the $ZnSO_4$−CFTA−H_2O electrolyte is negatively shifted, compared with that of the $ZnSO_4$−H_2O electrolyte, confirming the specific adsorption of Cl^- on the surface of the Zn crystal. To further substantiate the specific adsorption of Cl^- on the (002) crystal facet, we conducted differential capacitance curve measurements, as shown in Figure S6, using high (002) preferentially oriented Zn and polycrystalline commercial Zn anodes as the working electrodes. To avoid influence from Zn^{2+}, Na_2SO_4−H_2O, and Na_2SO_4−NaCl−H_2O were employed as electrolytes, respectively. The results demonstrated that the highest capacitance values were observed when Zn foil with a (002) preferential orientation was used in Na_2SO_4−NaCl−H_2O electrolyte. In contrast, commercial polycrystalline Zn foil exhibited the lowest capacitance in the Na_2SO_4−H_2O electrolyte. This phenomenon is primarily due to the smaller radius of Cl^-, compared to H_2O molecules, which reduces the thickness of

https://doi.org/10.1021/acsnano.3c10394
ACS Nano 2024, 18, 4932−4943

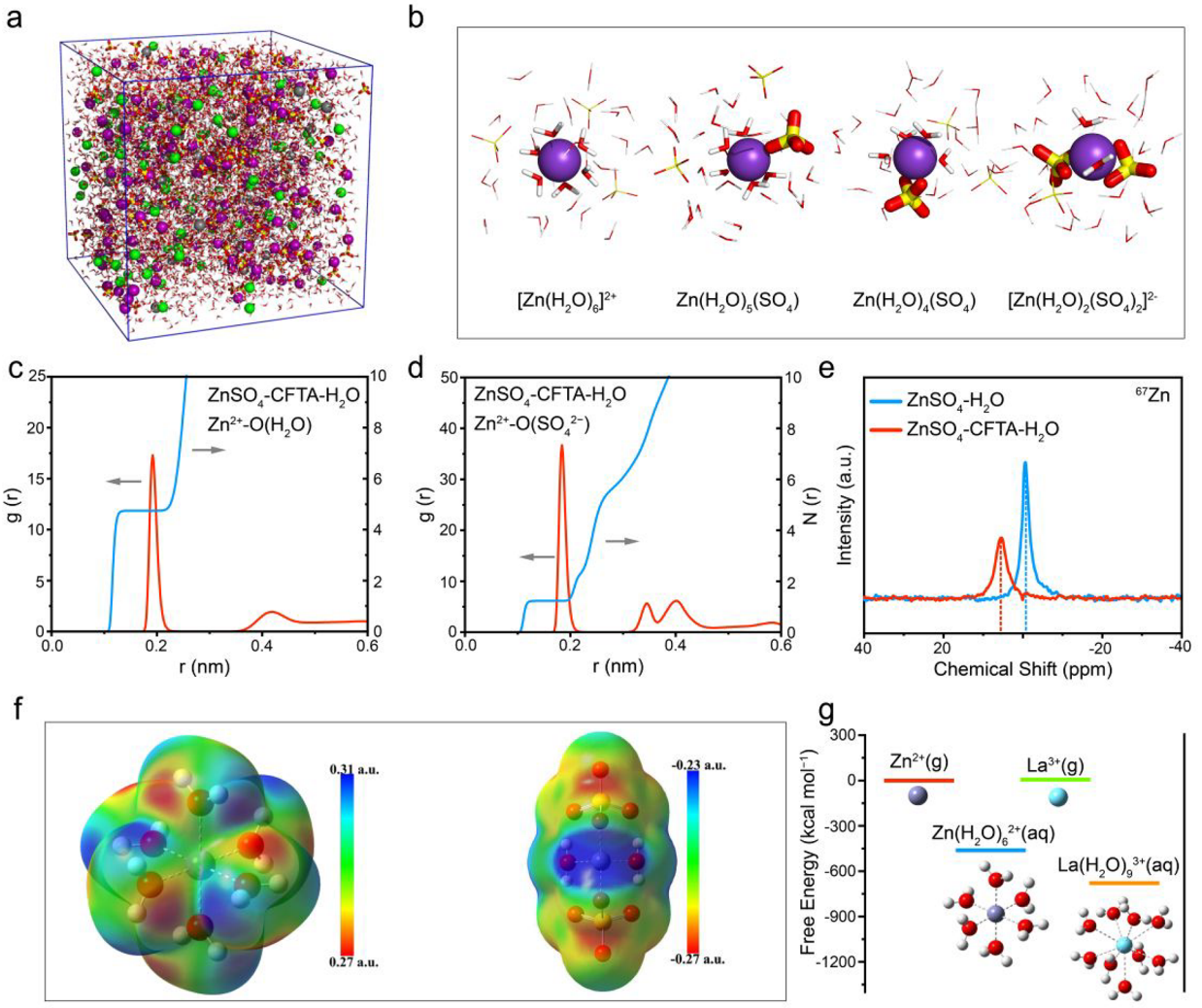

Figure 3. (a) 3D snapshot of $ZnSO_4$−CFTA−H_2O system. (b) Partial enlarged snapshot representing Zn^{2+} solvation structure in $ZnSO_4$−CFTA−H_2O system. (c) RDFs for Zn^{2+}−O (H_2O) and (d) Zn^{2+}−O (SO_4^{2-}) collected from MD simulations in $ZnSO_4$−CFTA−H_2O electrolyte. (e) ^{67}Zn NMR spectra in $ZnSO_4$−H_2O system and $ZnSO_4$−CFTA−H_2O system, respectively. (f) Electrostatic potential mapping of the original Zn^{2+}−$6H_2O$ (left) and Zn^{2+}−$2H_2O$−$2SO_4^{2-}$ (right) solvation structures. (g) Solvation energy of different ions.

the electric double layer, leading to an increase in capacitance. This further demonstrates the specific adsorption of Cl^- on the (002) surface. The highest concentration of La^{3+} and the lowest concentration of Zn^{2+} at the inner interface of the (002) facet indicate that La^{3+} and Zn^{2+} are competing to enter the innermost layer to compensate for the negative charge of Cl^- ions on the Zn (002) facet. Specifically, La^{3+} has a significantly lower reduction potential (−2.38 V vs standard hydrogen electrode (SHE)), compared to that of Zn^{2+} (−0.76 V vs standard hydrogen electrode). Therefore, when Zn^{2+} are reduced to Zn metal, it leads to further aggregation of La^{3+}, which, in turn, repels the adsorption of subsequent Zn^{2+} and reduces the growth rate of Zn (002) facet.

According to the MD simulation, the selective adsorption of Cl^- and La^{3+} on the Zn (002) facet is the intrinsic determinant of the formation of the Zn (002) texture. This specific adsorption makes the (002) facet grow slowly and be preferentially exposed, which is the crystal facet inhibition theory proposed at the beginning. To further substantiate the validity of this theory, the adsorption free energy of Cl^- on different crystal facets was calculated through density functional theory (DFT), as depicted in Figure 2e. Cl^- exhibits the highest adsorption free energy (−1.92 eV) on the Zn (002) facet, significantly surpassing that on the Zn(101) facet (−0.68 eV) and the Zn(110) facet (−1.25 eV). The difference of adsorption free energy of Cl^- on (002) and (101) facets is as high as 1.24 eV, which confirms that Cl^- can achieve specific adsorption and high coverage on the Zn(002) facet. This is consistent with MD simulation results, validating that the specific effect of CFTA on the (002) facet is primarily attributed to the high adsorption energy.

To thoroughly investigate the impact of CFTA on Zn electrocrystallization behavior, cyclic voltammetry (CV) tests were carried out (Figure S7). The electrodes selected for the experiments were Zn(101) highly preferred crystal, Zn polycrystal, and Zn(002) highly preferred crystal. Quantitatively, the peak intensity ratio of (101) to (002) in the Zn(101) highly preferred crystal is 12.3, while the peak intensity ratio of (002) to (101) in the Zn(002) highly preferred crystal is 16.67, as illustrated in Figure S8. In detail, the deposition potential of polycrystalline Zn is −0.98 V (vs SCE) in 2 M $ZnSO_4$ electrolyte (Figure S9). In contrast, the deposition potential on (101) highly preferred crystal, polycrystalline Zn and (002) highly preferred crystal substrates

https://doi.org/10.1021/acsnano.3c10394
ACS Nano 2024, 18, 4932−4943

gradually shifted negatively to −0.99, −1.01, and −1.03 V (vs SCE) in the $ZnSO_4$−CFTA−H_2O electrolyte, respectively. This is mainly because Cl^- forms an anion adsorption layer in the internal interface layer on the Zn(002) facet. The adsorption layer forms a double electric layer at the electrode−solution interface, facilitating the accumulation of positively charged La^{3+} on the (002) facet and resulting in a more negative deposition potential. Combined with the results of MD simulation and DFT, it is inferred that the robust specific adsorption capacity of Cl^- enhances the deposition potential of Zn on the (002) facet and attenuates the growth rate of the (002) facets.

To discern the texture characteristics of the Zn crystal, the hexagonal zinc deposit cut by focused ion beam (FIB) was observed under a high-resolution transmission electron microscopy (HRTEM) analysis. Note that the majority of lattice spacings on the surface of the deposit are 0.247 nm, which has been identified as (002) plane of Zn (Figure 2f), demonstrating a pronounced preferred orientation of the (002) crystal plane. The lattice fringes of (100) and (101) planes are clearly observed in the zinc anode with pure $ZnSO_4$ electrolyte, demonstrating the selectivity-free orientations (Figure 2g). To further emphasize the crystallographic orientation of zinc deposition process, X-ray diffraction pole figure analysis was employed. The (002) pole figure of Zn, obtained after circulation in the $ZnSO_4$−CFTA−H_2O electrolyte (Figure 2h), exhibits a significantly high intensity of 9.04. This suggests that the circulated Zn crystal possesses a pronounced texture predominantly aligned along the (002) facet and is nearly parallel to the electrode substrate. Differently, the Zn(002) pole diagram after circulation in the $ZnSO_4$−H_2O electrolyte exhibits anisotropy (Figure 2i), revealing a random (nonpreferred) process. Moreover, the XRD spectra indicate that the relative intensity ratio of the (002) peak to the (101) peak of Zn crystals deposited in the $ZnSO_4$−CFTA−H_2O electrolyte reaches 2.21 (Figure 2j), while in the $ZnSO_4$−H_2O electrolyte, the intensity ratio of the (002) crystal facet to the (101) crystal plane is 0.59, indicating a smaller proportion of the (002) facet exposure area. This suggests that Zn deposition in the $ZnSO_4$−CFTA−H_2O electrolyte exhibits a highly oriented (002) crystal facet, attributed to the synergistic effect of dual ions in CFTA. Additionally, distinct peaks corresponding to $Zn_4SO_4(OH)_6\cdot 5H_2O$ (PDF File No. 00-039-0688) are observed on the Zn anode after cycling in the $ZnSO_4$−H_2O electrolyte, which is ascribed to the side reactions between the Zn anode and the electrolyte.[29] In contrast, the peak of the byproduct is greatly inhibited in the $ZnSO_4$−CFTA−H_2O electrolyte. To demonstrate the inhibitory effect of CFTA on byproducts, we immersed Zn metal samples in $ZnSO_4$−H_2O and $ZnSO_4$−CFTA−H_2O electrolytes for 48 h and subsequently characterized their surfaces using SEM and XRD (Figure S10). SEM analysis revealed that a considerable number of flakelike byproducts formed on the Zn surface in $ZnSO_4$−H_2O electrolyte, while in $ZnSO_4$−CFTA−H_2O, the surface remained relatively smooth and uniform with no obvious byproducts. Further XRD comparative analysis showed significant peaks for byproducts on the Zn surface in $ZnSO_4$−H_2O, whereas the Zn samples treated in $ZnSO_4$−CFTA−H_2O exhibited very weak peaks for surface byproducts. This indicates that the addition of CFTA effectively suppresses the formation. Summarily, the dual ions in the $ZnSO_4$−CFTA−H_2O electrolyte coregulate the kinetics of crystal growth, suppress side reactions, and realize the preferential exposure of the (002) crystal facet for achieving dendrite-free Zn anodes.

MD simulations were performed in the bulk phase of $ZnSO_4$−H_2O and $ZnSO_4$−CFTA−H_2O systems to gain deeper insights into the inhibitory effect of CFTA electrolyte on byproducts (Figure 3a and Figure S11), respectively. The statistical results reveal that the primary solvation shell (PSS) of Zn^{2+} in 2 M $ZnSO_4$ electrolyte is predominantly composed of 5 or 6 H_2O molecules, as depicted in Figure S12. As a comparison, in the $ZnSO_4$−CFTA−H_2O electrolyte, four primary solvation structures were observed (Figure 3b), wherein the incorporation of two SO_4^{2-} ions into the PSS to replace the original H_2O molecules was observed, leading to a partial transformation of specific Zn^{2+} ions from a hexacoordinated state to a tetracoordinated state. This indicates that the addition of CFTA reconstructs the solvation structure of Zn^{2+} in an electrolyte.

The corresponding radial distribution function (RDF) and coordination number analysis in the electrolyte models are analyzed. In the $ZnSO_4$−H_2O electrolyte (Figure S13), the Zn−O peak at ∼2 Å from Zn^{2+} is attributed to the H_2O molecules in the PSS. Similarly, in the $ZnSO_4$−CFTA−H_2O system, the Zn−O peak corresponding to SO_4^{2-} and H_2O appears at ∼2 Å from Zn^{2+}, as depicted in Figures 3c and 3d, suggesting that some SO_4^{2-} enter the PSS. Furthermore, the average coordination number (ACN) of Zn−O (H_2O) and Zn−O (SO_4^{2-}) in PSS of the $ZnSO_4$−CFTA−H_2O system is ∼4.75 and 1.22 (right Y-axis of Figures 3c and 3d), respectively. This led to a reduction of 0.25 water molecules in the first solvation shell of Zn ions. More solvation structure information was uncovered by ^{67}Zn nuclear magnetic resonance (NMR) spectroscopy (Figure 3e). The ^{67}Zn chemical shift in the $ZnSO_4$−CFTA−H_2O system shifts to a lower field, indicating a reduction in the electron cloud density in the solvation layer of Zn^{2+}. Even though the electron cloud density of oxygen (O) in SO_4^{2-} is higher than that in H_2O molecules, as illustrated in Figure 3f, the low coordination number of Zn^{2+} results in a lower total electron cloud density (approximately −1.42) of Zn in the $ZnSO_4$−CFTA−H_2O system compared to the total electron cloud density (approximately −3.576) in the $ZnSO_4$−H_2O system. This indicates that the average coordination number of Zn^{2+} in the $ZnSO_4$−CFTA−H_2O electrolyte is lower, as evidenced by the lower total electron cloud density in the PSS of Zn^{2+}. The specific charge distribution information is depicted in Figure S14. These results demonstrate that the addition of CFTA alters the solvation structure of Zn^{2+} and reduces the proportion of H_2O molecules in PSS. The reduction of the proportion of H_2O molecules in the solvated structure can greatly inhibit the hydrogen evolution reaction (HER) and Zn anode corrosion.

The solvation energies of La^{3+} and Zn^{2+} in aqueous solution were further calculated by using DFT (Figure 3g). This calculation was performed to investigate the effect of low-concentration inorganic additives on the solvation structure of Zn^{2+}. The solvation energy of La^{3+} (−796 kcal mol^{-1}) is much higher than that of Zn^{2+} (−388 kcal mol^{-1}), indicating a stronger binding energy between La^{3+} and H_2O molecules. Moreover, the PSS of La^{3+} ion contains 9 H_2O molecules (Figure S15), implying that La^{3+} can regulate the solvation structure of Zn^{2+} in dilute electrolyte due to its high solvation energy and coordination number. In the $ZnSO_4$−CFTA−H_2O

https://doi.org/10.1021/acsnano.3c10394
ACS Nano 2024, 18, 4932−4943

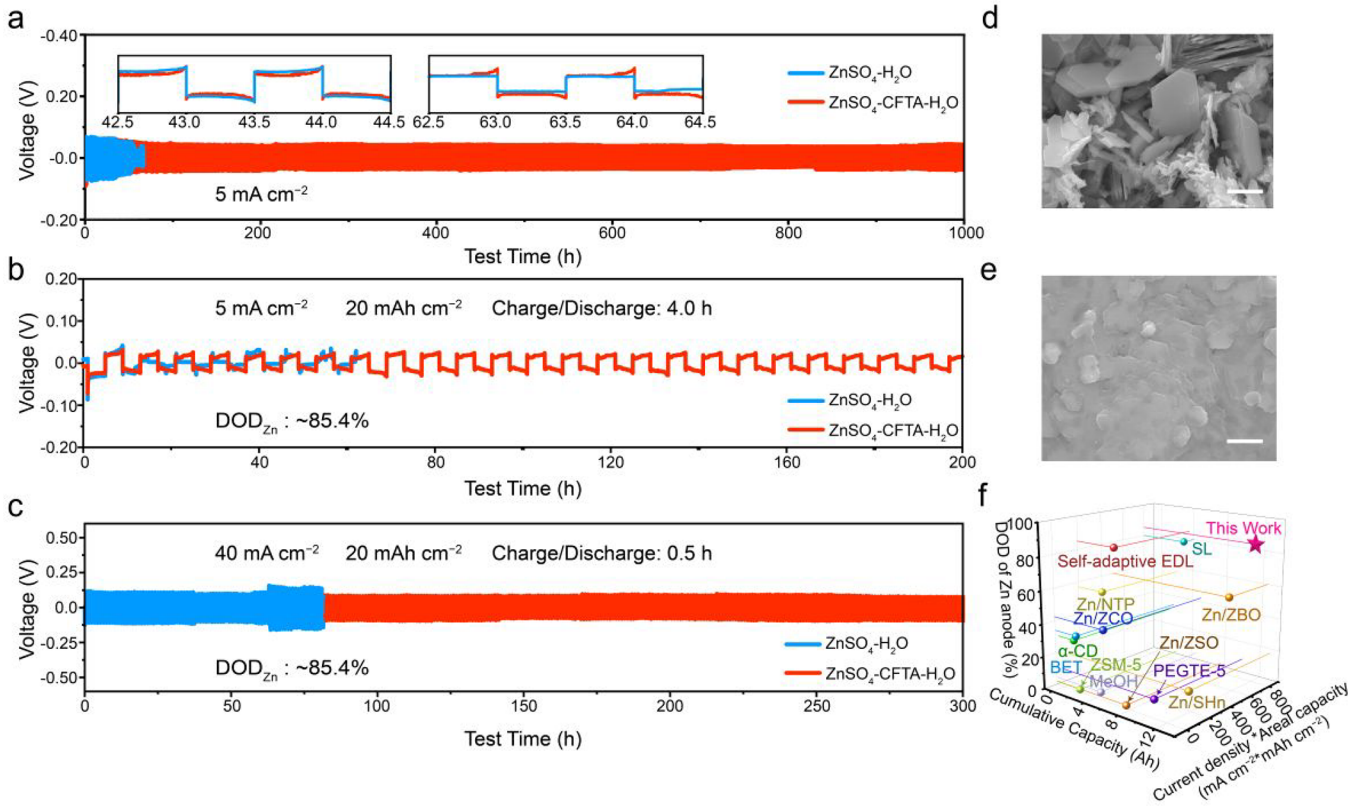

Figure 4. Galvanostatic Zn plating/stripping in Zn||Zn symmetrical cells at (a) 5 mA cm^{-2}, 2.5 mAh cm^{-2}, (b) 5 mA cm^{-2}, 20 mAh cm^{-2}, and (c) 40 mA cm^{-2}, 20 mAh cm^{-2}. SEM images of Zn anode after cycling at 40 mA cm^{-2} in (d) ZnSO$_4$−H$_2$O electrolyte and (e) ZnSO$_4$−CFTA−H$_2$O electrolyte. Scale bar: 1 μm. (f) The property comparison of Zn||Zn cell between this work and other reports. The detailed references corresponding to the point number are listed in Table S2, Supporting Information.

electrolyte, the number of H_2O molecules in the first solvation shell of La^{3+} is reduced to 7.69 (Figure S16), and the detailed solvation structure of La^{3+} in the $ZnSO_4$−CFTA−H_2O system is shown in Tables S3−S5. Specifically, Zn^{2+} in the vicinity of La^{3+} are unable to effectively compete for enough H_2O molecules, allowing SO_4^{2-} to readily enter the PSS and replace the original H_2O molecules. In summary, the proposed CFTA additive can not only regulate the growth kinetics of Zn crystals, generate Zn(002) texture, but also regulate the solvation structure of Zn^{2+}, reduce the proportion of active H_2O molecules in Zn^{2+} solvation, and inhibit the side reactions.

The Zn plating/stripping CE in two electrolytes were quantified using asymmetric Zn||Cu half-cells (Figure S17). High CE is a key indicator for achieving long-term cycling and high-areal-capacity battery. In the $ZnSO_4$−H_2O electrolyte, the Zn||Cu half-cell ran for only 80 cycles with a low average CE of approximately 98.9% at 1 mAh cm^{-2}, 5 mA cm^{-2}, which is due to the generation of dendrites and byproducts. In sharp contrast, the Zn||Cu half-cell utilizing the $ZnSO_4$−CFTA−H_2O electrolyte achieves a higher average CE of approximately 99.52% with stability over 500 cycles, attributed to the formation of planar Zn deposition and effective suppression of side reactions. The nucleation overpotential curves, as illustrated in Figure S17b and Figure S17c, show that the nucleation overpotential for Zn deposition in $ZnSO_4$−CFTA−H_2O and $ZnSO_4$−H_2O electrolytes are 32.5 and 33 mV, respectively, with minimal difference between them. This indicates that the electrostatic repulsion caused by La^{3+} aggregated on the (002) crystal facet does not increase the nucleation overpotential for Zn deposition. Next, to evaluate the stability of Zn anodes in two electrolytes, the Zn||Zn symmetric cells were tested in the range of 1 to 40 mA cm^{-2}. The Zn||Zn symmetric cells using $ZnSO_4$−CFTA−H_2O electrolyte exhibit significantly improved cycling stability, capable of stable operation for 2300 h at 1 mA cm^{-2} and 1 mAh cm^{-2} (Figure S18), which is nearly 17 times longer than that in $ZnSO_4$−H_2O electrolyte. Even at a higher current density of 5 mA cm^{-2} and higher areal capacity of 2.5 mAh cm^{-2}, it could still operate stably for over 1000 h (Figure 4a), with a voltage hysteresis of no more than 110 mV. Meanwhile, in $ZnSO_4$−H_2O electrolyte, it can only operate for 53 h. Such excellent cycling performance is attributed to the CFTA additive, which prevents the formation of dendrites during repeated Zn plating/stripping.

To assess its feasibility in realistic application scenarios, we conducted high-areal-capacity plating/stripping tests under harsh conditions with limited Zn supply (~15 μm). Under a current density of 5 mA cm^{-2} and a discharge capacity of 20 mAh cm^{-2}, a charging and discharging cycle takes 8 h. In the $ZnSO_4$−H_2O electrolyte, symmetric Zn||Zn cells can cycle only stably for 1 cycle, after which the cell fails due to severe Zn dendrite growth (Figure 4b). As a strong contrast, the Zn||Zn cells using $ZnSO_4$−CFTA−H_2O electrolyte and a limited Zn supply (~40 μm) exhibit a smaller voltage hysteresis (66 mV) and stable cycling lifespan (200 h) at 5 mA cm^{-2} and 20 mAh cm^{-2} (Figure 4b). Moreover, under more harsh conditions of an ultrahigh current density of 40 mA cm^{-2}, high areal capacity of 20 mAh cm^{-2}, and high DOD_{Zn} of 85.4%, the symmetric Zn||Zn cells employing $ZnSO_4$−CFTA−H_2O electrolyte still

https://doi.org/10.1021/acsnano.3c10394
ACS Nano 2024, 18, 4932−4943

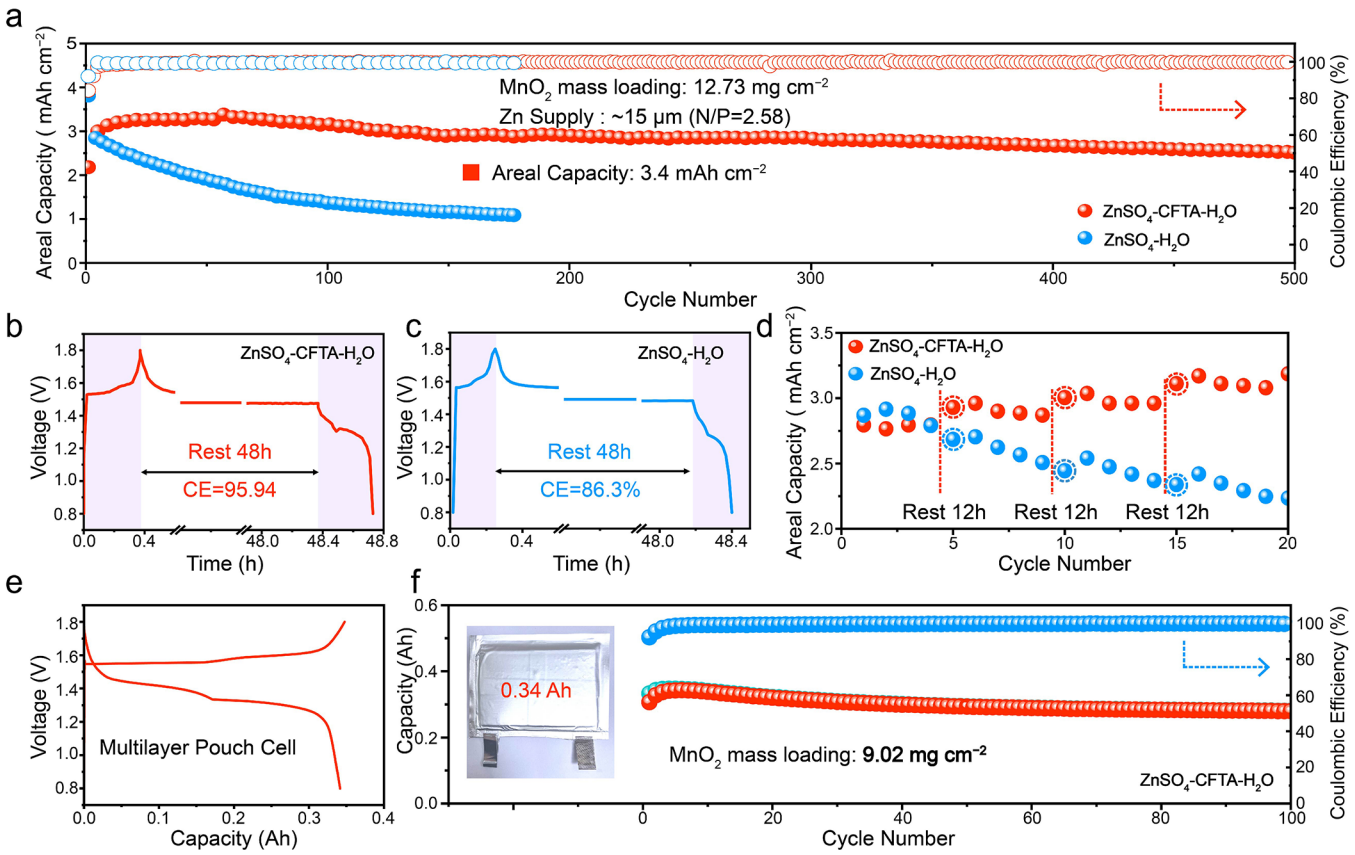

Figure 5. (a) Long-term cycling performance of Zn||MnO_2 coin cells at 1 C. (b, c) Stay performance of the full Zn||MnO_2 cell in $ZnSO_4$−CFTA−H_2O electrolyte (panel (b)) and $ZnSO_4$−H_2O electrolyte (panel (c)). (d) Stay-cycling performance of the full Zn||MnO_2 cell in $ZnSO_4$−H_2O electrolyte and $ZnSO_4$−CFTA−H_2O electrolyte, respectively. (e) Voltage profiles and (f) cycling performance of multilayer Zn||MnO_2 pouch cell using $ZnSO_4$−CFTA−H_2O electrolyte. The inset of panel (f) is the optical image of the multilayer Zn||MnO_2 pouch cell.

manifest a stable cycling over 300 h without apparent irreversible voltage observed (Figure 4c); meanwhile, the symmetric Zn||Zn cells using $ZnSO_4$−H_2O electrolyte show high hysteresis voltage (~230 mV) and rapidly encountered short-circuiting (80 h). SEM images of post-cycling Zn anodes in Figure 4c show that the Zn deposition layers are completely different when using different electrolytes. It exhibits an uneven and porous morphology with distinct tiplike structures for $ZnSO_4$−H_2O electrolyte (Figure 4d), whereas a dense and horizontally arranged platelike morphology is observed for $ZnSO_4$−CFTA−H_2O electrolyte (Figure 4e). This confirms that the Zn horizontal electrodeposition facilitated by the CFTA additive is prevalent during cycling of high DOD_{Zn} and long stability. Encouragingly, such ultrahigh cumulative capacity of 12 Ah with a high DOD (~85.4%) in this work are superior to most previously reported values for the aqueous Zn anodes (Figure 4f).[30−41] Additionally, we examined the rate performance of Zn||Zn symmetric cells using $ZnSO_4$−CFTA−H_2O electrolytes, as shown in Figure S20. Compared to symmetric cells with the $ZnSO_4$−H_2O electrolyte, there was no notable difference in polarization at low current densities. However, with increasing current density and prolonged time, the pure $ZnSO_4$ electrolyte exhibited greater polarization voltage due to more severe side reactions and hydrogen evolution. Therefore, attributed to the precise regulation of the Zn crystal facet and the inhibition of dendrite growth by CFTA additives, the Zn||Zn symmetric cells can exhibit excellent cycling performance at both high DOD and high areal capacity.

To identify the practical application of this facile strategy, a high mass loading (~9 mg cm^{-2} to 12.73 mg cm^{-2}) MnO_2 cathode was selected to couple with limited Zn anode (~15 μm) to fabricate a full Zn metal battery. CV curves were tested at a scan rate of 0.2 mV s^{-1} to evaluate the electrochemical property of the MnO_2 cathode in different electrolytes (Figure S23). MnO_2 cathode shows similar behavior in both electrolytes, in which two pairs of obvious Mn-ion redox peaks correspond to the stepwise transformation of Mn^{4+}/Mn^{3+} and Mn^{3+}/Mn^{2+}, which is consistent with the previous report.[42] Besides, at the same scanning rate, the full battery using the $ZnSO_4$−CFTA−H_2O electrolyte exhibits a larger peak current density and smaller polarization than that in the full battery using the pure $ZnSO_4$−H_2O electrolyte, which indicates that the Zn||MnO_2 battery using the $ZnSO_4$−CFTA−H_2O electrolyte has higher specific capacity and faster charge transfer.

As for the long-term cycling performance test, the capacity ratio of the negative electrode to the positive electrode (N/P) is a crucial parameter in the industrialization of Zn metal battery. In previous studies, most of systems select excessive Zn foil (≥150 μm) as an anode to couple with a low-mass-loading cathode (from 1 mg cm^{-2} to 2 mg cm^{-2}) to fabricate a full battery.[40] The N/P capacity ratio reported in these studies is usually higher than 50, which causes the Zn anode to have a low DOD_{Zn} and concomitant low energy density during the operation of the full battery. In our work, we set harsh test conditions to achieve deep Zn plating/stripping in anode. The

https://doi.org/10.1021/acsnano.3c10394
ACS Nano 2024, 18, 4932−4943

high-mass-loading of the MnO_2 positive electrode is 12.73 mg cm^{-2} and the Zn supply (~8.78 mAh cm^{-2}) is limited. As illustrated in Figure 5a, the full Zn||MnO_2 battery using $ZnSO_4$−H_2O electrolyte exhibits an area capacity of 3.82 mAh cm^{-2} at a current density of 308 mAh g^{-1} (1 C), and then the capacity dramatically decays to 1.09 mAh cm^{-2} only after 177 cycles (with 67.15% initial capacity retained). Inversely, the full Zn||MnO_2 battery (N/P capacity ratio: 2.58) using $ZnSO_4$−CFTA−H_2O electrolyte possesses a high areal capacity of 3.39 mAh cm^{-2} and retain a capacity of 2.52 mAh cm^{-2} after 500 cycles. Compared to previous data, our work has the highest cumulative capacity (up to 1.439 Ah cm^{-2}) under harsh test conditions, demonstrating a promising potential for practical Zn metal batteries.[43−45] Besides, the self-discharge behavior of the full battery was explored by using pure $ZnSO_4$ electrolyte and $ZnSO_4$−CFTA−H_2O electrolyte, respectively. After the full battery stands for 2 days, the full battery using the $ZnSO_4$−CFTA−H_2O electrolyte maintains 95.94% of its original capacity (Figure 5b), which is much better than the full battery (86.3%) using pure $ZnSO_4$ electrolyte (Figure 5c). These results again prove that dual-ion CFTA electrolyte can inhibit the parasitic reaction of the full battery.

To closely mimic practical conditions and evaluate the effect of the resting process on the long-term cycling performance, we performed resting-cycling tests. After 12 h of rest, as shown in Figure 5d, the battery using pure $ZnSO_4$−H_2O electrolyte exhibits noticeable capacity decay. The significant reduction in capacity after resting can be attributed to the continuous corrosion of irregularly deposited nanosized Zn during the resting process, which consumes a large amount of electrolyte and generates byproducts such as $Zn_4SO_4(OH)_6{\cdot}5H_2O$. This leads to a decrease in the effective contact area between the electrolyte and the positive electrode, resulting in rapid capacity deterioration. Note that the capacity of the full cell with $ZnSO_4$−CFTA−H_2O electrolyte slightly increases after a 12-h period of resting (Figure 5d). This is primarily due to the highly (002)-oriented Zn generated during the electrochemical deposition process, which has the lowest surface energy and the highest hydrogen evolution reaction (HER) barrier,[46] effectively inhibiting side reactions at the negative electrode−electrolyte interface. Limited side reactions occur during the resting period, and the resting process allows the electrolyte to fully infiltrate the high-mass-loading thick electrode, resulting in not only no reduction in the positive electrode capacity but also the electrolyte undergoing further activation. To further evaluate the application potential of the dual-ion CFTA electrolyte, the Zn||MnO_2 multilayer pouch cells were assembled for device demonstration. The high-mass-loading (9.02 mg cm^{-2}) MnO_2 positive electrode is fixed on the titanium mesh collector by the rolling method, coupled with the Zn foil, and the glass fiber is used as the separator. All layers are assembled into electric cores, which are clamped in the middle and sealed with aluminum plastic film by thermal sealing. As shown in Figures 5e and 5f, the Zn||MnO_2 pouch cell exhibits a maximum capacity of 343.2 mAh at a current density of 1 C. After 100 cycles, it still manifests a high-capacity retention rate of 91.3%. The high-capacity and stable pouch cells demonstrate that the $ZnSO_4$−CFTA−H_2O electrolyte has great potential for large-scale and practical application.

CONCLUSIONS

In summary, we propose a CFTA electrolyte strategy that can effectively alter the growth kinetics of Zn crystals and achieve the preferential growth of the Zn(002) facet, as evidenced by MD, DFT and electrochemical tests. In detail, the specific adsorption of the dual-ions terminating agent on the (002) facet diminishes the growth rate of the (002) facet, wherein the substantial adsorption free energy of Cl^- on the (002) facet and the simultaneous aggregation of La^{3+} ions play a pivotal role. The resultant electrostatic repulsion force reduces the accumulation of Zn^{2+} on the (002) facet, making it the slowest growing crystal facet and ultimately preserving it to form texture. Hence, the symmetric Zn||Zn cells employing $ZnSO_4$−CFTA−H_2O electrolyte demonstrate a prolonged cycling stability of 300 h at 40 mA cm^{-2} and 20 mAh cm^{-2}, along with a significant Zn utilization rate of 85.4%. Moreover, the full Zn||MnO_2 battery (N/P capacity ratio = 2.58) using $ZnSO_4$−CFTA−H_2O electrolyte, high-mass-loading MnO_2 cathode (12.73 mg cm^{-2}) and limited Zn foil (~15 μm) can cycle stably for 500 cycles at a current density of 1 C and the Zn||MnO_2 multilayer pouch cell delivers a capacity of 0.34 Ah. This facile strategy provides a insight into the preparation of highly preferred oriented Zn anodes and is promising for the commercial application of Zn metal batteries.

METHODS

Materials. $ZnSO_4$ (99.5%), $LaCl_3$ (99.9%), deionized (DI) water, $KMnO_4$ (99.0%), $Zn(NO_3)_2{\cdot}6H_2O$ (99.0%), and H_2SO_4 (98.0%) were purchased from Sinopharm. MnO_2 nanowires were prepared based on a facile hydrothermal method. Typically, 1.264 g of $KMnO_4$, 2.379 g of $ZnNO_3{\cdot}6H_2O$, and 2 mL of H_2SO_4 were mixed in 75 mL of DI water under continuous stirring for 20 min at room temperature. Subsequently, the mixture was transferred into a 100-mL Teflon-lined stainless-steel autoclave and maintained at 140 °C for 3.5 h. Finally, MnO_2 powder was obtained after being washed thoroughly with DI water and dried at 70 °C for 24 h.

Electrochemical Test. Zn||Zn symmetrical cell and full coin-type cells were tested in a CR2032 coin cell by multichannel battery testing system (LAND CT2001A). For the $ZnSO_4$−CFTA−H_2O electrolyte, 2 mol of $ZnSO_4$ and 0.3 mol of $LaCl_3$ were dissolved in 1 L of DI water. The amount of electrolyte we use in coin cells, symmetrical batteries, and pouch cells is 40 μL cm^{-2}. Additionally, we utilized a glass fiber separator, GFD, with a thickness of 675 μm. Pouch cells were test on Neware battery test system (Model CT-4008-5 V6A-S1-F, Shenzhen, China). For the cathode electrode, MnO_2 nanowire, CNT, and polytetrafluoroethylene (PTFE) binder were mixed with a weight ratio of 7:2:1. The slurry was grinned onto a Ti mesh and vacuum-dried at 70 °C for 24 h. The mass loading of the cathode electrodes was ~12.73 mg cm^{-2}. The anode electrodes were employed by five-cycle CV analysis at 0.2 mV s^{-1} within the potential window 0f 0.6−1.9 V. Zn foil was cut into disk shapes with a diameter of 12 mm as anode electrodes. Glass fiber film (GF/D, Whatman) was used as the separator. In the Zn||MnO_2 full battery, both electrolytes were supplemented with 0.2 M $MnSO_4$ additive. CV tests were carried out by using the electrochemical workstation (EC-LAB), and the voltage range for full cells was 0.8−1.8 V.

Characterizations. The morphology was conducted by scanning electron microscopy (SEM) (JEOL, Model JSM-7100F) and transmission electron microscopy (TEM) (JEOL, Model JEM-F200). The SEM measurement was taken using a JEOL Model JSM-7100F system with an acceleration voltage of 20 kV. The XRD data were collected on a Bruker Model D8 Advance X-ray diffractometer by using Cu Kα radiation (λ = 1.5418 Å). To avoid the influence of the zinc substrate on the deposits, we conducted the test using the tape stripping method in the XRD test. The ^{67}Zn NMR experiments were carried out with a Bruker Avance 400 system, using

https://doi.org/10.1021/acsnano.3c10394
ACS Nano 2024, 18, 4932−4943

5-mm tubes. XRD pole figures were done using X'Pert3MRD. Focused ion beam (FIB) analysis was performed on a FEI Scios 2 HiVac to cut hexagonal zinc deposits for TEM measurement.

MD Simulation. The atomistic force field parameters for all ions and water molecule are described by the AMBER format obtained from previous work.[47] The SPC/E water model is adopted in this work for atomistic simulations. The cross-interaction parameters between different atom types are obtained from the Lorentz−Berthelot combination rule.

Atomistic simulations were performed using the GROMACS package with cubic periodic boundary conditions. The detailed simulation system compositions are listed in Table 1. The equations for the motion of all atoms were integrated using a classic Verlet leapfrog integration algorithm with a time step of 1.0 fs. A cutoff radius of 1.6 nm was set for short-range van der Waals interactions and real-space electrostatic interactions. The particle-mesh Ewald (PME) summation method with an interpolation order of 5 and a Fourier grid spacing of 0.20 nm was employed to handle long-range electrostatic interactions in reciprocal space. All simulation systems were first energetically minimized using a steepest descent algorithm and thereafter annealed gradually from 600 K to room temperature (300 K) within 10 ns. All annealed simulation systems were equilibrated in an isothermal−isobaric (NPT) ensemble for 20 ns of physical time maintained using a Nosé−Hoover thermostat and a Parrinello−Rahman barostat with time coupling constants of 0.4 and 0.2 ps, respectively, to control the temperature at 300 K and the pressure at 1 atm. Atomistic simulations were further performed in a canonical ensemble (NVT) for 100 ns, and simulation trajectories were recorded at an interval of 100 fs for further structural and dynamical analysis.

DFT Calculation. Quantum chemical calculations were performed using the Gaussian 16 package[48] to optimize molecular geometries of representative solvation structures and thereafter to calculate binding energies of water molecules with La^{3+} and Zn^{2+} ions. The Beck's three-parameter hybrid functional with the Lee−Yang−Parr correlation functional (B3LYP) was used in computations. The LanL2DZ basis set was used for La^{3+} and Zn^{2+} ions, and the 6-311+G (d, p) basis set was applied to H, O, and Cl atoms. The molecular electrostatic potential contours around the optimized molecular geometries were obtained from quantum chemical calculations.

ASSOCIATED CONTENT

Supporting Information

The Supporting Information is available free of charge at https://pubs.acs.org/doi/10.1021/acsnano.3c10394.

In situ optical microscopy images of Zn deposition on the negative side in Zn||Zn symmetric systems; CV test of different Zn facets in a three-electrode system; XRD patterns of Zn polycrystal, Zn (101) highly preferred crystal, and Zn (002) highly preferred crystal, respectively; 3D snapshot, Zn^{2+} solvation structure, La^{3+} solvation structure, RDFs for Zn^{2+}−O (H_2O) obtained from MD simulations (PDF)

AUTHOR INFORMATION

Corresponding Author

Lin Xu − *State Key Laboratory of Advanced Technology for Materials Synthesis and Processing, School of Materials Science and Engineering, Wuhan University of Technology, Wuhan 430070, China; Hubei Longzhong Laboratory, Wuhan University of Technology (Xiangyang Demonstration Zone), Xiangyang 441000, People's Republic of China;* orcid.org/0000-0003-2347-288X; Email: linxu@whut.edu.cn

Authors

Qin Liu − *State Key Laboratory of Advanced Technology for Materials Synthesis and Processing, School of Materials Science and Engineering, Wuhan University of Technology, Wuhan 430070, China*

Xiong Liu − *School of Materials Science and Engineering, Zhengzhou University, Zhengzhou 450001, People's Republic of China*

Yu Liu − *State Key Laboratory of Advanced Technology for Materials Synthesis and Processing, School of Materials Science and Engineering, Wuhan University of Technology, Wuhan 430070, China*

Meng Huang − *State Key Laboratory of Advanced Technology for Materials Synthesis and Processing, School of Materials Science and Engineering, Wuhan University of Technology, Wuhan 430070, China*

Weihao Wang − *State Key Laboratory of Advanced Technology for Materials Synthesis and Processing, School of Materials Science and Engineering, Wuhan University of Technology, Wuhan 430070, China*

Yu Cheng − *State Key Laboratory of Advanced Technology for Materials Synthesis and Processing, School of Materials Science and Engineering, Wuhan University of Technology, Wuhan 430070, China*

Hong Zhang − *State Key Laboratory of Advanced Technology for Materials Synthesis and Processing, School of Materials Science and Engineering, Wuhan University of Technology, Wuhan 430070, China*

Complete contact information is available at: https://pubs.acs.org/10.1021/acsnano.3c10394

Author Contributions

The manuscript was written through contributions of all authors. All authors have given approval to the final version of the manuscript.

Notes

The authors declare no competing financial interest.

ACKNOWLEDGMENTS

This work was supported the National Natural Science Foundation of China (Nos. 52272234, 52172233, 52127816), the National Key Research and Development Program of China (No. 2020YFA0715000), the Key Research and Development Program of Hubei Province (No. 2021BAA070), Independent Innovation Projects of the Hubei Longzhong Laboratory (No. 2022ZZ-20), the Sanya Science and Education Innovation Park of Wuhan University of Technology (No. 2021KF0011) and the China Postdoctoral Science Foundation (No. 2022M722856).

REFERENCES

(1) Parker, J. F.; Chervin, C. N.; Pala, I. R.; Machler, M.; Burz, M. F.; Long, J. W.; Rolison, D. R. Rechargeable nickel-3D zinc batteries: An energy-dense, safer alternative to lithium-ion. *Science* **2017**, *356*, 415−418.

(2) Ma, L.; Schroeder, M. A.; Borodin, O.; Pollard, T. P.; Ding, M. S.; Wang, C.; Xu, K. Realizing high zinc reversibility in rechargeable batteries. *Nat. Energy* **2020**, *5*, 743−749.

(3) Yin, Y.; Wang, S.; Zhang, Q.; Song, Y.; Chang, N.; Pan, Y.; Zhang, H.; Li, X. Dendrite-Free Zinc Deposition Induced by Tin-Modified Multifunctional 3D Host for Stable Zinc-Based Flow Battery. *Adv. Mater.* **2020**, *32*, 1906803.

(4) Zheng, X.; Liu, Z.; Sun, J.; Luo, R.; Xu, K.; Si, M.; Kang, J.; Yuan, Y.; Liu, S.; Ahmad, T.; et al. Constructing robust heterostructured interface for anode-free zinc batteries with ultrahigh capacities. *Nat. Commun.* **2023**, *14*, 3278.
(5) Gong, Z.; Li, Z.; Wang, P.; Jiang, K.; Bai, Z.; Zhu, K.; Yan, J.; Ye, K.; Wang, G.; Cao, D.; Chen, G. Conductive Framework-Stabilized Zn-Metal Anodes for High-Performance Zn-Ion Batteries and Capacitors. *Energy Mater. Adv.* **2023**, *4*, No. 0035.
(6) Ma, L.; Chen, S.; Long, C.; Li, X.; Zhao, Y.; Liu, Z.; Huang, Z.; Dong, B.; Zapien, J. A.; Zhi, C. Achieving High-Voltage and High-Capacity Aqueous Rechargeable Zinc Ion Battery by Incorporating Two-Species Redox Reaction. *Adv. Energy Mater.* **2019**, *9*, 1902446.
(7) Xiong, F.; Jiang, Y.; Cheng, L.; Yu, R.; Tan, S.; Tang, C.; Zuo, C.; An, Q.; Zhao, Y.; Gaumet, J.-J.; Mai, L. Low-strain TiP_2O_7 withthree-dimensionalionchannelsas long-life and high-rate anode material for Mg-ion batteries. *Interdiscip. Mater.* **2022**, *1*, 140.
(8) Cao, P.; Zhou, X.; Wei, A.; Meng, Q.; Ye, H.; Liu, W.; Tang, J.; Yang, J. Fast-Charging and Ultrahigh-Capacity Zinc Metal Anode for High-Performance Aqueous Zinc-Ion Batteries. *Adv. Funct. Mater.* **2021**, *31*, 2100398.
(9) Zeng, Y.; Zhang, X.; Qin, R.; Liu, X.; Fang, P.; Zheng, D.; Tong, Y.; Lu, X. Dendrite-Free Zinc Deposition Induced by Multifunctional CNT Frameworks for Stable Flexible Zn-Ion Batteries. *Adv. Mater.* **2019**, *31*, 1903675.
(10) Xing, Z. Y.; Sun, Y. Y.; Xie, X. S.; Tang, Y.; Xu, G. F.; Han, J. W.; Lu, B. A.; Liang, S. Q.; Chen, G.; Zhou, J. Zincophilic Electrode Interphase with Appended Proton Reservoir Ability Stabilizes Zn Metal Anodes. *Angew. Chem., Int. Ed.* **2023**, *62*, e202215324.
(11) Liang, G.; Zhu, J.; Yan, B.; Li, Q.; Chen, A.; Chen, Z.; Wang, X.; Xiong, B.; Fan, J.; Xu, J.; Zhi, C. Gradient fluorinated alloy to enable highly reversible Zn-metal anode chemistry. *Energy Environ. Sci.* **2022**, *15*, 1086−1096.
(12) Yang, Y.; Liu, C.; Lv, Z.; Yang, H.; Zhang, Y.; Ye, M.; Chen, L.; Zhao, J.; Li, C. C. Synergistic Manipulation of Zn^{2+} Ion Flux and Desolvation Effect Enabled by Anodic Growth of a 3D ZnF_2 Matrix for Long-Lifespan and Dendrite-Free Zn Metal Anodes. *Adv. Mater.* **2021**, *33*, 2007388.
(13) Zheng, J. X.; Zhao, Q.; Tang, T.; Yin, J. F.; Quilty, C. D.; Renderos, G. D.; Liu, X. T.; Deng, Y.; Wang, L.; Bock, D. C.; Jaye, C.; Zhang, D. H.; Takeuchi, E. S.; Takeuchi, K. J.; Marschilok, A. C.; Archer, L. A. Reversible epitaxial electrodeposition of metals in battery anodes. *Science* **2019**, *366*, 645−655.
(14) Zhou, M.; Guo, S.; Li, J.; Luo, X.; Liu, Z.; Zhang, T.; Cao, X.; Long, M.; Lu, B.; Pan, A.; et al. Surface-Preferred Crystal Plane for a Stable and Reversible Zinc Anode. *Adv. Mater.* **2021**, *33*, 2100187.
(15) Qiu, M. J.; Sun, P.; Wang, Y.; Ma, L.; Zhi, C. Y.; Mai, W. J. Anion-Trap Engineering toward Remarkable Crystallographic Reorientation and Efficient Cation Migration of Zn Ion Batteries. *Angew. Chem., Int. Ed.* **2022**, *61*, e202210979.
(16) Ma, L.; Li, Q.; Ying, Y.; Ma, F.; Chen, S.; Li, Y.; Huang, H.; Zhi, C. Toward Practical High-Areal-Capacity Aqueous Zinc-Metal Batteries: Quantifying Hydrogen Evolution and a Solid-Ion Conductor for Stable Zinc Anodes. *Adv. Mater.* **2021**, *33*, 2007406.
(17) Huang, Y. The discovery of cathode materials for lithium-ion batteries from the view of interdisciplinarity. *Interdiscip. Mater.* **2022**, *1*, 323−329.
(18) Zeng, X. H.; Mao, J. F.; Hao, J. N.; Liu, J. T.; Liu, S. L.; Wang, Z. J.; Wang, Y. Y.; Zhang, S. L.; Zheng, T.; Liu, J. W.; Rao, P. H.; Guo, Z. P. Electrolyte Design for In Situ Construction of Highly Zn^{2+}-Conductive Solid Electrolyte Interphase to Enable High-Performance Aqueous Zn-Ion Batteries under Practical Conditions. *Adv. Mater.* **2021**, *33*, 2007416.
(19) Cao, L. S.; Li, D.; Deng, T.; Li, Q.; Wang, C. S. Hydrophobic Organic-Electrolyte-Protected Zinc Anodes for Aqueous Zinc Batteries. *Angew. Chem., Int. Ed.* **2020**, *59*, 19292−19296.
(20) Zhu, Y. P.; Yin, J.; Zheng, X. L.; Emwas, A. H.; Lei, Y. J.; Mohammed, O. F.; Cui, Y.; Alshareef, H. N. Concentrated dual-cation electrolyte strategy for aqueous zinc-ion batteries. *Energy Environ. Sci.* **2021**, *14*, 4463−4473.
(21) Li, C.; Shyamsunder, A.; Hoane, A. G.; Long, D. M.; Kwok, C. Y.; Kotula, P. G.; Zavadil, K. R.; Gewirth, A. A.; Nazar, L. F. Highly reversible Zn anode with a practical areal capacity enabled by a sustainable electrolyte and superacid interfacial chemistry. *Joule* **2022**, *6*, 1103−1120.
(22) Yang, J.; Zhao, R.; Wang, Y.; Bai, Y.; Wu, C. Regulating Uniform Zn Deposition via Hybrid Artificial Layer for Stable Aqueous Zn-Ion Batteries. *Energy Mater. Adv.* **2022**, *2022*, 9809626.
(23) Hoang, T. K. A.; Doan, T. N. L.; Cho, J. H.; Su, J. Y. J.; Lee, C.; Lu, C.; Chen, P. Sustainable Gel Electrolyte Containing Pyrazole as Corrosion Inhibitor and Dendrite Suppressor for Aqueous Zn/$LiMn_2O_4$ Battery. *ChemSusChem* **2017**, *10*, 2816−2822.
(24) Li, N.; Li, G. Q.; Li, C. J.; Yang, H. C.; Qin, G. W.; Sun, X. D.; Li, F.; Cheng, H. M. Bi-Cation Electrolyte for a 1.7 V Aqueous Zn Ion Battery. *ACS Appl. Mater. Interfaces* **2020**, *12*, 13790−13796.
(25) Jin, Y.; Han, K. S.; Shao, Y. Y.; Sushko, M. L.; Xiao, J.; Pan, H. L.; Liu, J. Stabilizing Zinc Anode Reactions by Polyethylene Oxide Polymer in Mild Aqueous Electrolytes. *Adv. Funct. Mater.* **2020**, *30*, 2003932.
(26) Li, D.; Cao, L. S.; Deng, T.; Liu, S. F.; Wang, C. S. Design of a Solid Electrolyte Interphase for Aqueous Zn Batteries. *Angew. Chem., Int. Ed.* **2021**, *60*, 13035−13041.
(27) Zhu, M. S.; Hu, J. P.; Lu, Q. Q.; Dong, H. Y.; Karnaushenko, D. D.; Becker, C.; Karnaushenko, D.; Li, Y.; Tang, H. M.; Qu, Z.; Ge, J.; Schmidt, O. G. A Patternable and In Situ Formed Polymeric Zinc Blanket for a Reversible Zinc Anode in a Skin-Mountable Microbattery. *Adv. Mater.* **2021**, *33*, 2007497.
(28) Frank, F. C.; Merwe, J. H. One-Dimensional Dislocations. II. Misfitting Monolayers and Oriented Overgrowth. *Proc. R. Soc. London* **1949**, *198*, 216−225.
(29) Du, H. R.; Zhao, R. R.; Yang, Y.; Liu, Z. K.; Qie, L.; Huang, Y. H. High-Capacity and Long-Life Zinc Electrodeposition Enabled by a Self-Healable and Desolvation Shield for Aqueous Zinc-Ion Batteries. *Angew. Chem.,, Int. Ed.* **2022**, *61*, e202114789.
(30) Wang, D.; Liu, H.; Lv, D.; Wang, C.; Yang, J.; Qian, Y. Rational Screening of Artificial Solid Electrolyte Interphases on Zn for Ultrahigh-Rate and Long-Life Aqueous Batteries. *Adv. Mater.* **2023**, *35*, 2207908.
(31) Lv, Y.; Zhao, M.; Du, Y.; Kang, Y.; Xiao, Y.; Chen, S. Engineering a self-adaptive electric double layer on both electrodes for high-performance zinc metal batteries. *Energy Environ. Sci.* **2022**, *15*, 4748−4760.
(32) Guo, R.; Liu, X.; Xia, F.; Jiang, Y.; Zhang, H.; Huang, M.; Niu, C.; Wu, J.; Zhao, Y.; Wang, X.; Han, C.; Mai, L. Large-Scale Integration of a Zinc Metasilicate Interface Layer Guiding Well-Regulated Zn Deposition. *Adv. Mater.* **2022**, *34*, 2202188.
(33) Zhang, Y.; Zheng, X.; Wu, K.; Zhang, Y.; Xu, G.; Wu, M.; Liu, H.; Dou, S.; Wu, C. Nonionic Surfactant-Assisted In Situ Generation of Stable Passivation Protective Layer for Highly Stable Aqueous Zn Metal Anodes. *Nano Lett.* **2022**, *22*, 8574−8583.
(34) Zhao, M.; Lv, Y. Q.; Zhao, S. S.; Xiao, Y.; Niu, J.; Yang, Q.; Qiu, J. S.; Wang, F.; Chen, S. M. Simultaneously Stabilizing Both Electrodes and Electrolytes by a Self-Separating Organometallics Interface for High-Performance Zinc-Ion Batteries at Wide Temperatures. *Adv. Mater.* **2022**, *34*, 2206239.
(35) Zhu, J.; Bie, Z.; Cai, X.; Jiao, Z.; Wang, Z.; Tao, J.; Song, W.; Fan, H. J. A Molecular-Sieve Electrolyte Membrane enables Separator-Free Zinc Batteries with Ultralong Cycle Life. *Adv. Mater.* **2022**, *34*, 2207209.
(36) Zhao, K.; Fan, G.; Liu, J.; Liu, F.; Li, J.; Zhou, X.; Ni, Y.; Yu, M.; Zhang, Y.; Su, H.; Liu, Q.; Cheng, F. Boosting the Kinetics and Stability of Zn Anodes in Aqueous Electrolytes with Supramolecular Cyclodextrin Additives. *J. Am. Chem. Soc.* **2022**, *144*, 11129−11137.
(37) Wang, M.; Ma, J.; Meng, Y.; Sun, J.; Yuan, Y.; Chuai, M.; Chen, N.; Xu, Y.; Zheng, X.; Li, Z.; Chen, W. High-Capacity Zinc Anode with 96% Utilization Rate Enabled by Solvation Structure Design. *Angew. Chem., Int. Ed.* **2023**, *62*, e202214966.
(38) Ren, H.; Li, S.; Wang, B.; Zhang, Y.; Wang, T.; Lv, Q.; Zhang, X.; Wang, L.; Han, X.; Jin, F.; et al. Molecular-Crowding Effect

Mimicking Cold-Resistant Plants to Stabilize the Zinc Anode with Wider Service Temperature Range. *Adv. Mater.* **2023**, *35*, 2208231.
(39) Wang, P.; Liang, S.; Chen, C.; Xie, X.; Chen, J.; Liu, Z.; Tang, Y.; Lu, B.; Zhou, J. Spontaneous Construction of Nucleophilic Carbonyl-Containing Interphase toward Ultrastable Zinc-Metal Anodes. *Adv. Mater.* **2022**, *34*, 2202733.
(40) Yang, J.; Li, J.; Zhao, J.; Liu, K.; Yang, P.; Fan, H. J. Stable Zinc Anodes Enabled by a Zincophilic Polyanionic Hydrogel Layer. *Adv. Mater.* **2022**, *34*, 2202382.
(41) Ma, L.; Vatamanu, J.; Hahn, N. T.; Pollard, T. P.; Borodin, O.; Petkov, V.; Schroeder, M. A.; Ren, Y.; Ding, M. S.; Luo, C.; et al. Highly reversible Zn metal anode enabled by sustainable hydroxyl chemistry. *Proc. Natl. Acad. Sci. U.S.A.* **2022**, *119*, e2121138119.
(42) Jiao, Y.; Kang, L.; Berry-Gair, J.; Mccoll, K.; Li, J.; Dong, H.; Jiang, H.; Wang, R.; Cora, F.; Dan, B.; et al. Enabling Stable MnO_2 Matrix for Aqueous Zinc-ion Battery Cathodes. *J. Mater. Chem. A* **2020**, *8*, 22075−22082.
(43) Cai, Z.; Wang, J.; Sun, Y. Anode corrosion in aqueous Zn metal batteries. *eScience* **2023**, *3*, 100093.
(44) Cao, L.; Li, D.; Pollard, T.; Deng, T.; Zhang, B.; Yang, C.; Chen, L.; Vatamanu, J.; Hu, E.; Hourwitz, M. J.; et al. Fluorinated interphase enables reversible aqueous zinc battery chemistries. *Nat. Nanotechnol.* **2021**, *16*, 902.
(45) Bayaguud, A.; Luo, X.; Fu, Y.; Zhu, C. Cationic Surfactant-Type Electrolyte Additive Enables Three-Dimensional Dendrite-Free Zinc Anode for Stable Zinc-Ion Batteries. *ACS Energy Lett.* **2020**, *5*, 3012−3020.
(46) Zhou, M.; Guo, S.; Li, J. L.; Luo, X. B.; Liu, Z. X.; Zhang, T. S.; Cao, X. X.; Long, M. Q.; Lu, B. G.; Pan, A. Q.; et al. Surface-Preferred Crystal Plane for a Stable and Reversible Zinc Anode. *Adv. Mater.* **2021**, *33*, 2007416.
(47) Wang, Y.-L.; Shah, F. U.; Glavatskih, S.; Antzutkin, O. N.; Laaksonen, A. Atomistic insight into orthoborate-based ionic liquids: Force field development and evaluation. *J. Phys. Chem. B* **2014**, *118*, 8711−8723.
(48) Frisch, M.; Trucks, G. W.; Schlegel, H. B.; Scuseria, G. E.; Robb, M. A.; Cheeseman, J. R.; Scalmani, G.; Barone, V.; Petersson, G. A.; Nakatsuji, H.; Li, X.; Caricato, M.; Marenich, A. V.; Bloino, J.; Janesko, B. G.; Gomperts, R.; Mennucci, B.; Hratch, D. J. *Gaussian 16, Revision C.01*; Gaussian, Inc., Wallingford, CT, 2016.

https://doi.org/10.1021/acsnano.3c10394
ACS Nano 2024, 18, 4932−4943